



RIOJA. JWST and ALMA Unveil the Inhomogeneous and Complex Interstellar Medium Structure in a Star-forming Galaxy at $z = 6.81$

Downloaded from: <https://research.chalmers.se>, 2026-04-13 23:41 UTC




















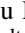

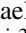

Citation for the original published paper (version of record):

Usui, M., Mawatari, K., Álvarez-Márquez, J. et al (2025). RIOJA. JWST and ALMA Unveil the Inhomogeneous and Complex Interstellar Medium Structure in a Star-forming Galaxy at $z = 6.81$. *Astrophysical Journal Letters*, 991(2).
<http://dx.doi.org/10.3847/2041-8213/ae0574>

N.B. When citing this work, cite the original published paper.



RIOJA. JWST and ALMA Unveil the Inhomogeneous and Complex Interstellar Medium Structure in a Star-forming Galaxy at $z = 6.81$

Mitsutaka Usui¹, Ken Mawatari^{1,2,3,4} , Javier Álvarez-Márquez⁵ , Takuya Hashimoto^{1,4} , Yuma Sugahara^{2,3} ,
Rui Marques-Chaves⁶ , Akio K. Inoue^{2,3} , Luis Colina⁵ , Santiago Arribas⁵ , Carmen Blanco-Prieto⁵ ,
Yurina Nakazato⁷ , Naoki Yoshida^{7,8,9} , Tom J. L. C. Bakx^{10,11,12} , Daniel Ceverino^{13,14} , Luca Costantin⁵ ,
Alejandro Crespo Gómez¹⁵ , Masato Hagimoto¹¹ , Hiroshi Matsuo^{16,17} , Wataru Osone¹ , Yi W. Ren³ ,
Yoshinobu Fudamoto¹⁸ , Takeshi Hashigaya¹⁹ , Miguel Pereira-Santaella²⁰ , and Yoichi Tamura¹¹ 

¹ Division of Physics, Faculty of Pure and Applied Sciences, University of Tsukuba, Tsukuba, Ibaraki 305-8571, Japan; hashimoto.takuya.ga@u.tsukuba.ac.jp

² Waseda Research Institute for Science and Engineering, Faculty of Science and Engineering, Waseda University, 3-4-1 Okubo, Shinjuku, Tokyo 169-8555, Japan

³ Department of Pure and Applied Physics, School of Advanced Science and Engineering, Faculty of Science and Engineering, Waseda University, 3-4-1 Okubo, Shinjuku, Tokyo 169-8555, Japan

⁴ Tomonaga Center for the History of the Universe (TCHoU), Faculty of Pure and Applied Sciences, University of Tsukuba, Tsukuba, Ibaraki 305-8571, Japan

⁵ Centro de Astrobiología (CAB), CSIC-INTA, Ctra. de Ajalvir km 4, Torrejón de Ardoz, E-28850, Madrid, Spain

⁶ Geneva Observatory, Department of Astronomy, University of Geneva, Chemin Pegasi 51, CH-1290 Versoix, Switzerland

⁷ Department of Physics, The University of Tokyo, 7-3-1 Hongo, Bunkyo, Tokyo 113-0033, Japan

⁸ Kavli Institute for the Physics and Mathematics of the Universe (WPI), UT Institute for Advanced Study, The University of Tokyo, Kashiwa, Chiba 277-8583, Japan

⁹ Research Center for the Early Universe, School of Science, The University of Tokyo, 7-3-1 Hongo, Bunkyo, Tokyo 113-0033, Japan

¹⁰ Department of Space, Earth, & Environment, Chalmers University of Technology, Chalmersplatsen 4 412 96 Gothenburg, Sweden

¹¹ Department of Physics, Graduate School of Science, Nagoya University, Nagoya 464-8602, Japan

¹² National Astronomical Observatory of Japan, 2-21-1, Osawa, Mitaka, Tokyo 181-8588, Japan

¹³ Universidad Autónoma de Madrid, Ciudad Universitaria de Cantoblanco, E-28049 Madrid, Spain

¹⁴ CIAFF, Facultad de Ciencias, Universidad Autónoma de Madrid, E-28049 Madrid, Spain

¹⁵ Space Telescope Science Institute (STScI), 3700 San Martin Drive, Baltimore, MD 21218, USA

¹⁶ National Astronomical Observatory of Japan, 2-21-1 Osawa, Mitaka, Tokyo 181-8588, Japan

¹⁷ Graduate University for Advanced Studies (SOKENDAI), 2-21-1 Osawa, Mitaka, Tokyo 181-8588, Japan

¹⁸ Center for Frontier Science, Chiba University, 1-33 Yayoi-cho, Inage-ku, Chiba 263-8522, Japan

¹⁹ Department of Astronomy, Kyoto University Sakyo-ku, Kyoto 606-8502, Japan

²⁰ Instituto de Física Fundamental (IFF), CSIC, Serrano 123, E-28006, Madrid, Spain

Received 2025 July 2; revised 2025 September 9; accepted 2025 September 9; published 2025 September 29

Abstract

We report the discovery of a complex density-stratified interstellar medium (ISM) in the star-forming galaxy COS-2987 at $z = 6.81$, revealed by the unprecedented synergy between James Webb Space Telescope (JWST)/NIRSpec integral field spectroscopy and Atacama Large Millimeter/submillimeter Array (ALMA) observations. These observations detect key emission lines, including [O II] $\lambda\lambda$ 3727, 3730, [O III] 4364, [O III] $\lambda\lambda$ 4960, 5008, and [O III] 88 μm , as well as $\text{H}\alpha$ and $\text{H}\beta$. JWST spectroscopy alone indicates ISM properties that are typical for galaxies at $z \sim 7$. These include low dust extinction ($A_V \approx 0.14$ mag), moderate electron density ($n_e \approx 500 \text{ cm}^{-3}$), and low gas-phase metallicity ($\sim 10\%$). However, the strong far-infrared [O III] 88 μm emission detected by ALMA cannot be explained by a single-component ionized medium with uniform electron density and temperature. Instead, a two-component ISM model—comprising compact, high-temperature, and high-density gas components ($T_e \approx 26,000 \text{ K}$; $n_e \approx 600 \text{ cm}^{-3}$) and an extended, cooler, and lower-density component ($T_e \approx 8000 \text{ K}$; $n_e \approx 50 \text{ cm}^{-3}$)—successfully reproduces the observed line ratios of [O III] 88 μm /[O III] 5008 \AA and [O III] 4364/[O III] 5008 \AA , with a volume ratio of 1 : 300 between the two components. Our results demonstrate that JWST alone probes only a fraction of the ISM and highlight the critical importance of combining JWST and ALMA to reveal the density-stratified ISM of early galaxies.


Unified Astronomy Thesaurus concepts: Galaxy formation (595); Galaxy evolution (594); Interstellar medium (847)

1. Introduction

Understanding the physical properties of the interstellar medium (ISM) in galaxies is crucial for studying galaxy formation and evolution. With the advent of the James Webb Space Telescope (JWST; J. P. Gardner et al. 2023) and the Atacama Large Millimeter/submillimeter Array (ALMA; A. Wootten & A. R. Thompson 2009), fundamental physical

quantities in H II regions—such as the electron density (n_e), electron temperature (T_e), ionization parameter, and gas-phase metallicity—can now be measured even in galaxies at redshifts (z) beyond 4 out to the epoch of reionization ($z \gtrsim 6$; e.g., Y. Isobe et al. 2023; M. Killi et al. 2023; K. Nakajima et al. 2023; Abdurro’uf et al. 2024; S. Arribas et al. 2024; I. H. Laseter et al. 2024; R. L. Sanders et al. 2024; J. Álvarez-Márquez et al. 2025; J. A. Zavala et al. 2025).

Recent studies have reported evidence for a density-stratified ISM in high- z galaxies based on emission-line diagnostics spanning the rest-frame ultraviolet (UV) and optical wavelengths. Specifically, n_e derived from high-ionization UV lines such as

 Original content from this work may be used under the terms of the [Creative Commons Attribution 4.0 licence](https://creativecommons.org/licenses/by/4.0/). Any further distribution of this work must maintain attribution to the author(s) and the title of the work, journal citation and DOI.

C III] $\lambda\lambda$ 1907, 1909 and N IV] $\lambda\lambda$ 1483, 1486²¹ often exceed 10^4 – 10^5 cm⁻³, while lower densities (10^2 – 10^3 cm⁻³) are inferred from optical diagnostics such as [O II] $\lambda\lambda$ 3727, 3730 or [S II] $\lambda\lambda$ 6718, 6733²² (e.g., M. Mingozzi et al. 2022; X. Ji et al. 2024; J. Álvarez-Márquez et al. 2025; M. W. Topping et al. 2025; A. Crespo Gómez et al. 2025, in preparation). This apparent discrepancy is interpreted as evidence for a density-stratified ISM, in which UV lines such as C III] and N IV] trace highly ionized, high-density regions, whereas optical lines like [O II] and [S II] originate from lower-ionization, lower-density gas.

A similar trend is also seen in the far-infrared (FIR) regime. Based on Herschel/PACS observations of LMC-N11, the second-largest giant H II region in the LMC after 30 Doradus, V. Lebouteiller et al. (2012) found that [O III] 88 μ m emission is spatially extended well beyond the area predicted from the number of massive stars. The emission requires low-density gas with $n_e < 16$ cm⁻³, which is much lower than the values inferred from optical [O II] and [S II] doublets (~ 100 cm⁻³) or [Cl III] $\lambda\lambda$ 5517, 5538 (~ 1700 cm⁻³). They interpreted this as evidence that [O III] 88 μ m emission is photoionized by far-UV photons that penetrate into low-density regions due to a clumpy ISM structure.

Motivated by these findings, we investigate whether a similar stratification of highly ionized gas can be identified by combining rest-frame optical and FIR [O III] emission lines.²³

In principle, one can determine both T_e and n_e of an H II region with uniform physical conditions using emission lines of [O III]. For example, the flux ratio of [O III] 5008 Å/4364 Å depends primarily on T_e , whereas the flux ratio of [O III] 88 μ m/5008 Å depends on both T_e and n_e (e.g., H. L. Dinerstein et al. 1985; D. E. Osterbrock & G. J. Ferland 2006; L. J. Kewley et al. 2019; T. Jones et al. 2020; S. Yang & A. Lidz 2020; Y. Nakazato et al. 2023). This technique has recently been applied to local analogs of high- z galaxies to investigate ISM properties such as T_e , n_e , and elemental abundance ratios (e.g., Y. Chen et al. 2023, 2024; see also N. Kumari et al. 2024).

At $z \gtrsim 6$, the powerful synergy between JWST and ALMA enables, for the first time, complementary observations of rest-frame optical and FIR [O III] emission lines. S. Fujimoto et al. (2024), M. Stiavelli et al. (2023), and A. Harshan et al. (2024) have estimated n_e in $z \sim 8$ –9 galaxies based on measurements of T_e from optical spectroscopy and the flux ratio of [O III] 88 μ m/5008 Å. However, these studies utilized the NIRSpect multi-object spectroscopy (MOS) mode to observe optical [O III] emission lines, which are subject to uncertainties arising from slit-loss corrections and from effects related to the position angle, particularly when the high- z source has a clumpy morphology or is elongated along a specific axis. In contrast, ALMA observations are free from such observational limitations. To accurately characterize the global properties of galaxies, a combination of NIRSpect integral field spectroscopy

(IFS; T. Böker et al. 2022) and ALMA observations is a crucial next step (see, e.g., J. Scholtz et al. 2025; J. A. Zavala et al. 2025).

The Reionization and the ISM/Stellar Origins with JWST and ALMA (RIOJA) project (JWST GO1 PID 1840; PIs: J. Álvarez-Márquez and T. Hashimoto; T. Hashimoto et al. 2023; K. Mawatari et al. 2025; Y. Sugahara et al. 2025) conducts follow-up observations of 12 ALMA [O III] 88 μ m emitters using NIRSpect/IFS and NIRCAM. Here, we present a combined analysis of optical and FIR [O III] emission lines in COS-2987030247 (hereafter COS-2987; R. Smit et al. 2015, 2018; N. Laporte et al. 2017; J. Witstok et al. 2022; A. C. Posses et al. 2023; Y. Harikane et al. 2025a; K. Mawatari et al. 2025), a star-forming galaxy at $z = 6.81$. We find that a simple homogeneous ISM model cannot reproduce the observed [O III] line ratios, suggesting the presence of hidden complexity in the ionized-gas structure, such as multiple ionized-gas components with distinct physical conditions in terms of T_e and n_e .

In a companion paper (K. Mawatari et al. 2025), we provide an overview of the observations of COS-2987, discuss its stellar populations based on combined JWST and ALMA data, and present the ISM properties derived from JWST’s spatially resolved observations.

Throughout this Letter, we adopt a Λ CDM cosmology, with $\Omega_m = 0.3$, $\Omega_\Lambda = 0.7$, and $H_0 = 70$ km s⁻¹ Mpc⁻¹. We assume a solar luminosity of $L_\odot = 3.839 \times 10^{33}$ erg s⁻¹ and a solar metallicity of $12 + \log(\text{O}/\text{H})_\odot = 8.69$ (M. Asplund et al. 2009). Hereafter, [O II] $\lambda\lambda$ 3727, 3730, [O III] 4364 Å, [O III] $\lambda\lambda$ 4960, 5008, and [O III] 88 μ m are referred to as [O II] 3727, 3730, [O III] 4364, [O III] 4960, 5008, and [O III] 88, respectively, unless otherwise specified.

2. Observations and Data

2.1. JWST NIRSpect IFS Data

The JWST NIRSpect IFS data were obtained as part of the RIOJA project. The specific observations can be accessed via the Mikulski Archive for Space Telescopes at the Space Telescope Science Institute: [10.17909/6mmv-2944](https://archive.stsci.edu/10.17909/6mmv-2944). Details of the observations and data reduction procedures are presented in K. Mawatari et al. (2025). Briefly, we used the G395H/F290LP grating/filter combination, which provides a high spectral resolution ($R \sim 2700$) and covers a wavelength range from 2.87 to 5.27 μ m.

The raw data were processed using the JWST reduction pipeline, version 1.14.0 (H. Bushouse et al. 2024), under the CRDS context `rwst_1223.pmap`. We performed the following custom steps to improve the data quality: (1) sigma clipping, to reject bad pixels and cosmic rays; and (2) subtraction of the median background from the calibrated images (e.g., M. A. Marshall et al. 2023; M. Perna et al. 2023; H. Übler et al. 2023). The final data cube was combined using the “drizzle” method, sampled with a pixel size of $0''.05$. To ensure that the line fluxes are measured from the same spatial region, the point-spread function (PSF) of the cube was matched to that of the H α emission line, which corresponds to the longest wavelength among the detected lines (see Appendix A).

As presented in K. Mawatari et al. (2025), we detected multiple emission lines, including [O II] 3727, 3730, H β , [O III] 4364, [O III] 4960, 5008, and H α , all at $\gtrsim 4\sigma$ significance in the integrated spectrum. The left panel of Figure 1 shows the integrated intensity map of the [O III] 5008 emission, while the

²¹ C III] has an ionization potential of 24.4 eV, with critical densities of $\sim 8.7 \times 10^4$ and $\sim 2.8 \times 10^5$ cm⁻³ for $\lambda\lambda$ 1907, 1909, respectively. N IV] has a higher ionization potential of 47.5 eV and n_{crit} values of $\sim 1.5 \times 10^5$ and $\sim 5.0 \times 10^5$ cm⁻³ for $\lambda\lambda$ 1483, 1486 (e.g., D. E. Osterbrock & G. J. Ferland 2006).

²² [O II] has an ionization potential of 13.6 eV, with critical densities of $\sim 1.4 \times 10^3$ and $\sim 3.4 \times 10^3$ cm⁻³ for $\lambda\lambda$ 3727, 3730, respectively. [S II] has an ionization potential of 10.4 eV and n_{crit} values of $\sim 1.5 \times 10^3$ and $\sim 3.9 \times 10^3$ cm⁻³ for $\lambda\lambda$ 6718, 6733 (e.g., D. E. Osterbrock & G. J. Ferland 2006).

²³ [O III] has an ionization potential of 35.1 eV, and critical densities of 3.0×10^6 , 6.8×10^7 , and 510 cm⁻³ for $\lambda\lambda$ 4364 Å, λ 5008 Å, and 88 μ m, respectively (e.g., D. E. Osterbrock & G. J. Ferland 2006).

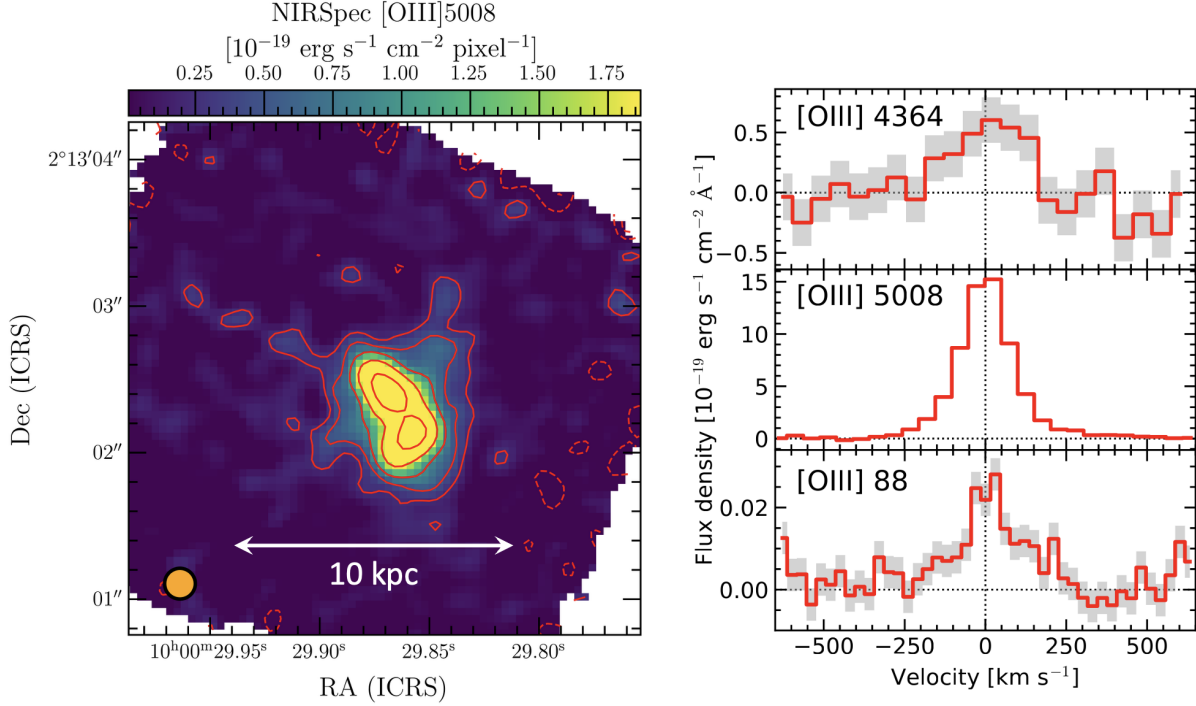


Figure 1. Left: integrated intensity map of the NIRSpec [O III] 5008 emission. The red contours show the $\pm 2^n \sigma$ significance levels ($n = 1, 2, 3, \dots$), where $\sigma = 1.16 \times 10^{-20} \text{ erg s}^{-1} \text{ cm}^{-2} \text{ pixel}^{-1}$. Positive and negative contours are shown by the solid and dashed lines, respectively. The orange circle at the bottom left indicates the FWHM of $0\farcs21$ at the observed wavelength of $\text{H}\alpha$ ($5.125 \mu\text{m}$). Right: one-dimensional spectra of [O III] 4364, [O III] 5008, and [O III] 88, where the horizontal axis is the velocity relative to the best-fit redshift to the [O III] 5008 line. In each panel, the red solid histogram and gray shade indicate the observed flux density and 1σ uncertainty, respectively. The gray shade is not visible for [O III] 5008, due to its negligible 1σ uncertainty.

spatially integrated one-dimensional spectra of [O III] 4364 and [O III] 5008 are shown in the right panel.

Table 1 shows the line fluxes. The fluxes were obtained by applying Gaussian fitting to each line profile, where the spectra were extracted from regions with $\gtrsim 2\sigma$ significance in the [O III] 5008 intensity map (Figure 1). Based on a curve-of-growth analysis, we estimate that the adopted aperture misses $\approx 10\%$ of the total flux. Therefore, we applied a 10% aperture correction to all line flux values, because we use the PSF-matched data. This aperture correction does not affect the line ratios of the NIRSpec IFS data, but it is required when comparing NIRSpec IFS and ALMA data.

2.2. ALMA [O III] 88 μm Data

ALMA Band 8 (Y. Sekimoto et al. 2008)²⁴ observations targeting [O III] 88 in COS-2987 were conducted as part of an ALMA Cycle 6 program (ID: 2018.1.00429.S; PI: R. Smit). Although J. Witstok et al. (2022) presented the initial detection and results of the [O III] 88 line, we reanalyzed the data cube to uniformly measure the line flux of COS-2987 in a manner consistent with other RIOJA studies.

The data were reduced using the Common Astronomy Software Applications (CASA; CASA Team et al. 2022) version 5.6. Imaging was performed with the CASA `tclean` task, adopting natural weighting to optimize point-source sensitivity. The final cube has a synthesized beam size of $0\farcs80 \times 0\farcs61$ with a positional angle of 86° , consistent with J. Witstok et al. (2022). The typical rms noise of the cube is $0.576 \text{ mJy beam}^{-1}$ per 30 km s^{-1} channel.

As shown in Figure B1 in Appendix B, we integrated the emission over the frequency range of 434.2–434.9 GHz, corresponding to a velocity width of 480 km s^{-1} (i.e., ≈ 3 times the FWHM of the optical lines), to generate the integrated intensity (moment-0) map of the [O III] 88 emission. The noise level of the map is $\sigma = 82.6 \text{ mJy beam}^{-1} \text{ km s}^{-1}$, and the [O III] 88 line is detected at a peak significance of 7.5σ . We measure an integrated line flux of $1.06 \pm 0.23 \text{ Jy km s}^{-1}$, corresponding to a flux of $(15.3 \pm 3.3) \times 10^{-18} \text{ erg s}^{-1} \text{ cm}^{-2}$, consistent with the values reported in J. Witstok et al. (2022) within uncertainties. The bottom right panel of Figure 1 shows the spectrum of [O III] 88 emission.

3. Properties Obtained from NIRSpec/IFS

3.1. Integrated Internal Dust Extinction

We estimate the internal dust extinction (A_V) of COS-2987 to correct the observed emission-line fluxes. We derive A_V based on the Balmer decrement of $\text{H}\alpha/\text{H}\beta$ as follows:²⁵

$$A_V = \frac{2.5 \times R_V}{k(\lambda_{\text{H}\beta}) - k(\lambda_{\text{H}\alpha})} \log_{10} \left[\frac{(\text{H}\alpha/\text{H}\beta)_{\text{obs}}}{(\text{H}\alpha/\text{H}\beta)_{\text{theo}}} \right], \quad (1)$$

where $k(\lambda)$ denotes the extinction curve, and $R_V \equiv A_V/E(B - V)$ is the total-to-selective extinction ratio. We adopt the SMC extinction curve with $R_V = 2.74$ (K. D. Gordon et al. 2003). $(\text{H}\alpha/\text{H}\beta)_{\text{obs}}$ and $(\text{H}\alpha/\text{H}\beta)_{\text{theo}}$ represent the observed

²⁴ See also T. Bakx & J. Conway (2024) for a summary of ALMA receiver references.

²⁵ At the sky position of the target and over the wavelength range of $\sim 3\text{--}5 \mu\text{m}$, the Galactic extinction is negligible ($A_\lambda < 0.01 \text{ mag}$; D. J. Schlegel et al. 1998).

Table 1
The Spatially Integrated Properties for COS-2987

Line Fluxes ^a (10^{-18} erg s $^{-1}$ cm $^{-2}$)	
$F_{[\text{O II}] 3727}$	7.1 ± 0.9
$F_{[\text{O II}] 3730}$	7.6 ± 1.2
$F_{[\text{O III}] 4364}$	1.8 ± 0.5
$F_{\text{H}\beta}$	8.0 ± 0.8
$F_{[\text{O III}] 4960}$	17.4 ± 1.8
$F_{[\text{O III}] 5008}$	52.3 ± 5.4
$F_{\text{H}\alpha}$	23.9 ± 2.4
$F_{[\text{O III}] 88}$	15.3 ± 3.3
Line Ratios ^b	
$\text{H}\alpha/\text{H}\beta$	3.00 ± 0.40
$[\text{O III}] 4364/5008$	$0.038^{+0.010}_{-0.011}$
$[\text{O II}] 3730/3727$	1.05 ± 0.21
$[\text{O II}] 3727,3730/\text{H}\beta$	$1.99^{+0.41}_{-0.37}$
$[\text{O III}] 4960,5008/\text{H}\beta$	$8.64^{+0.13}_{-0.09}$
$[\text{O III}] 88/5008^c$	$0.22^{+0.09}_{-0.07}$
Physical Properties	
A_V/mag	$0.14^{+0.32}_{-0.14}$
$T_e([\text{O III}])/\text{K}$	$2.02^{+0.30}_{-0.28} \times 10^4$
$T_e([\text{O II}])/\text{K}^d$	$1.72^{+0.21}_{-0.20} \times 10^4$
$n_e([\text{O II}])/\text{cm}^{-3}$	494^{+546}_{-300}
$12+\log(\text{O}/\text{H})$	$7.67^{+0.11}_{-0.13}$
Dust-corrected Line Luminosity [$\times 10^8 L_\odot$]	
$L_{[\text{O III}] 4364}$	$3.35^{+2.08}_{-1.17}$
$L_{[\text{O III}] 5008}$	$88.5^{+44.2}_{-17.2}$
$L_{[\text{O III}] 88}$	21.4 ± 4.6

Notes.

^a All values before the dust correction.

^b All values corrected by dust extinction, except the Balmer decrement, for which we present the observed value.

^c The $[\text{O III}] 88/5008$ ratio includes 10% absolute flux calibration uncertainties for both the $[\text{O III}] 5008$ and 88 fluxes (see Section 4).

^d Scaled from $T_e([\text{O III}])$ with Equation (2).

and theoretical Balmer-line ratios, respectively. We obtain $(\text{H}\alpha/\text{H}\beta)_{\text{obs}} = 3.00 \pm 0.40$ (Table 1).

To account for the dependence of $(\text{H}\alpha/\text{H}\beta)_{\text{theo}}$ on electron density and temperature, we perform an iterative calculation, following B. Welch et al. (2024), who carefully derived ISM properties for two high- z star-forming galaxies using data from the TEMPLATES JWST Early Release Science program (J. R. Rigby et al. 2025).²⁶ To estimate the uncertainty in A_V , we perform a Monte Carlo simulation with 10,000 realizations, randomly perturbing the observed $\text{H}\alpha$ and $\text{H}\beta$ fluxes within their uncertainties.

We find $A_V = 0.14^{+0.32}_{-0.14}$ mag. This result indicates that COS-2987 is dust-poor, consistent with the nondetection of

²⁶ We first calculate $(\text{H}\alpha/\text{H}\beta)_{\text{theo}}$ in Case B recombination, assuming an electron density of $n_e = 100 \text{ cm}^{-3}$ and an electron temperature of $T_e = 10^4 \text{ K}$, using the `PyNeb RecAtom` function (V. Luridiana et al. 2015). We then derive A_V from Equation (1), correct the observed emission-line fluxes for dust attenuation, and remeasure the electron density and temperature from the $[\text{O II}] 3730/3727$ and $[\text{O III}] 5008/4364$ line ratios, respectively. This process is repeated until the change in temperature between iterations becomes less than 10 K.

dust continuum emission by ALMA (R. Smit et al. 2018; J. Witstok et al. 2022). Hereafter, unless otherwise stated, we base our analysis on the dust-corrected line ratios in Table 1.

3.2. Electron Temperature

We measure the electron temperature of the highly ionized gas, $T_e([\text{O III}])$, based on the $[\text{O III}] 4364/5008$ line ratio, using the `PyNeb getTemDen` function (V. Luridiana et al. 2015). The uncertainty in $T_e([\text{O III}])$ is estimated via a Monte Carlo method, following the same approach as for A_V (Section 3.1). Based on the measured line ratio of $[\text{O III}] 4364/5008 = 0.038^{+0.010}_{-0.011}$ (Table 1), we derive an electron temperature of $T_e([\text{O III}]) = 2.02^{+0.30}_{-0.28} \times 10^4 \text{ K}$. This value is comparable to those found in other $z \sim 7$ galaxies with similar gas-phase metallicity to COS-2987 ($\approx 10\%$ of the solar metallicity; see Section 3.4) observed by JWST (e.g., D. Schaerer et al. 2022; K. Nakajima et al. 2023; J. E. Rhoads et al. 2023; M. Curti et al. 2024; I. H. Laseter et al. 2024; T. Morishita et al. 2024; R. L. Sanders et al. 2024).

We estimate the electron temperature of the lower-ionization gas, $T_e([\text{O II}])$, using the relation from A. Campbell et al. (1986) and G. Stasińska (1982):

$$T_e([\text{O II}]) = 0.7 \times T_e([\text{O III}]) + 3000 \text{ K}. \quad (2)$$

Applying this relation, we obtain $T_e([\text{O II}]) = 1.72^{+0.21}_{-0.20} \times 10^4 \text{ K}$.

3.3. Electron Density

We estimate the electron density based on the $[\text{O II}] 3730/3727$ line ratio, using the `PyNeb getTemDen` function (V. Luridiana et al. 2015). We adopt $T_e([\text{O II}])$ derived in Section 3.2, although the $[\text{O II}] 3730/3727$ ratio has a weak dependence on electron temperature. The uncertainty in $n_e([\text{O II}])$ is evaluated using a Monte Carlo method, following the same procedure as for A_V (Section 3.1). From the measured line ratio of $[\text{O II}] 3730/3727 = 1.05 \pm 0.21$ (Table 1), we derive an electron density of $n_e([\text{O II}]) = 494^{+546}_{-300} \text{ cm}^{-3}$.

Figure 2 shows the redshift evolution of the electron density, where the red star represents n_e of COS-2987. The n_e values at $z \sim 0-3$ in R. L. Davies et al. (2021) are derived from the $[\text{S II}]$ ratio, while those in R. L. Sanders et al. (2016) are obtained from either the $[\text{S II}]$ or $[\text{O II}]$ line ratios. Our measurement is consistent with typical values for $z \sim 5-10$ galaxies derived from the $[\text{O II}]$ ratio (Y. Isobe et al. 2023; Abdurro'uf et al. 2024; C. Marconcini et al. 2024), and also agrees with the best-fit redshift–electron density relation shown by the blue dashed line (Abdurro'uf et al. 2024). We stress that the data point of COS-2987 nicely falls in the redshift gap ($z \sim 6-8$) in the previous study of Y. Isobe et al. (2023).

3.4. Gas-phase Metallicity Based on the Direct T_e Method

We estimate the oxygen abundance, $12 + \log(\text{O}/\text{H})$, as a proxy for the gas-phase metallicity, using the direct T_e method with the `PyNeb getIonAbundance` function (V. Luridiana et al. 2015). We assume that the total oxygen abundance O/H is the sum of O^{++}/H^+ and O^+/H^+ . The O^{++}/H^+ abundance is estimated from the $[\text{O III}] 4960,5008/\text{H}\beta$ ratio and $T_e([\text{O III}])$, while the O^+/H^+ abundance is derived from the $[\text{O II}] 3727,3730/\text{H}\beta$ ratio and $T_e([\text{O II}])$ (Table 1).

The uncertainty in $12 + \log(\text{O}/\text{H})$ is evaluated using the same Monte Carlo technique adopted for A_V (Section 3.1). We obtain a metallicity of $12 + \log(\text{O}/\text{H}) = 7.67^{+0.11}_{-0.13}$, corresponding to $10\% \pm 2\%$ of the solar metallicity.

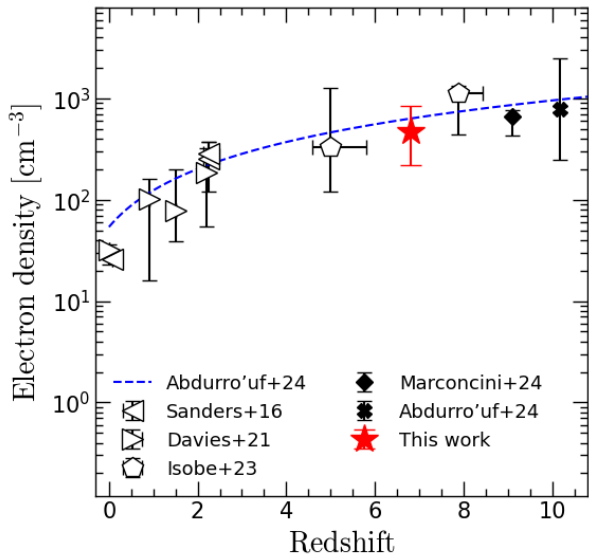


Figure 2. Redshift evolution of the electron density n_e . The red star indicates the electron density of COS-2987, derived from the [O II] ratio. Literature data at $z \sim 0-3$ are compiled from R. L. Sanders et al. (2016; [S II] or [O II]) and R. L. Davies et al. (2021; [S II]), while data at $z \gtrsim 4$ are taken from Y. Isobe et al. (2023), Abdurro’uf et al. (2024), and C. Marconcini et al. (2024), all based on the [O II] ratios. The filled symbols represent measurements for individual galaxies, and the open symbols represent median values for the sample galaxies. The electron density of COS-2987, derived from the [O II] ratio, is consistent with the overall redshift evolution trend indicated by the blue dashed line (Abdurro’uf et al. 2024).

4. [O III] Line Ratio Diagnostics Combining JWST and ALMA

One of the major strengths of this study is that we have four [O III] emission lines: the rest-frame optical emission lines of [O III] 4364 and [O III] 4960, 5008 observed with JWST/NIRSpec IFS, together with the rest-frame FIR emission line [O III] 88 observed with ALMA. Since these are emitted from the same ion of oxygen, we can derive the physical properties of nebulae without assumptions of abundance ratios.

The left panel of Figure 3 presents a diagnostic diagram of the optical [O III] line ratio ([O III] 4364/5008) versus the FIR-to-optical [O III] line ratio ([O III] 88/5008), overlaid with model grids covering a wide range of n_e and T_e values. These model grids are calculated with `PyNeb`, assuming that all [O III] lines originate from a homogeneous ionized gas with uniform electron temperature and density.

The red star in the left panel of Figure 3 shows the observed [O III] line ratios for COS-2987, where the [O III] 88/5008 ratio incorporates a 10% absolute flux calibration uncertainty for both [O III] 5008 (T. Böker et al. 2023)²⁷ and [O III] 88 (ALMA Cycle 6 Proposer’s Guide)²⁸.

For comparison, we also plot [O III] line ratios from the literature. The black filled symbols represent high- z star-forming galaxies. These include COS-3018 at $z = 6.85$ (R. Smit et al. 2018; J. Witstok et al. 2022; J. Scholtz et al. 2025), SXDF-NB1006-2 at $z = 7.21$ (A. K. Inoue et al. 2016; Y. W. Ren et al. 2023; Y. Harikane et al. 2025b; Y. W. Ren et al. 2025, submitted),

J0217-0208 at $z = 6.20$ (Y. Harikane et al. 2020, 2025b), and J1211-0118 at $z = 6.03$ (Y. Harikane et al. 2020, 2025b), where [O III] 4364 and [O III] 5008 were observed using the NIRSpec/IFS mode and [O III] 88 with ALMA. We additionally plot MACS0416-Y1 at $z = 8.38$ (T. J. L. C. Bakx et al. 2020; Y. Tamura et al. 2023; A. Harshan et al. 2024; M. Hagimoto et al. 2025), SMACS0723-04590 at $z = 8.50$ (S. Fujimoto et al. 2024), and MACS1149-JD1 at $z = 9.11$ (T. Hashimoto et al. 2018; T. Tokuoka et al. 2022; M. Stiavelli et al. 2023), where [O III] 4364 and [O III] 5008 were observed using the NIRSpec/MOS²⁹ mode and [O III] 88 with ALMA. The black open symbols show local dwarf galaxies, including Mrk 71 at a distance of 3.4 Mpc (Y. Chen et al. 2023), Pox 186 at $z = 0.0041$ (N. Kumari et al. 2024), and Haro 3 at $z = 0.0032$ (Y. Chen et al. 2024), where both the optical and FIR [O III] lines were observed with IFS.

In the left panel of Figure 3, the observed ratios for COS-2987, COS-3018, and J0217-0218 lie outside the T_e - n_e model grids, whereas the other high- z galaxies fall within the grids. Moreover, the high- z data points from the literature (black filled symbols) suggest $n_e = 100-500 \text{ cm}^{-3}$, while the redshift dependence presented in Figure 2 indicates typical densities of $n_e > 500 \text{ cm}^{-3}$. Therefore, the lower- n_e values from the FIR-to-optical [O III] line ratios seem to be common in high- z galaxies (see also a recent similar conclusion by Y. Harikane et al. 2025b).

We stress that the lower- n_e values derived from the FIR-to-optical [O III] ratios are not limited to high- z galaxies. As noted in Section 1, observations of the nearby massive star-forming region LMC-N11 reveal spatially extended and bright [O III] 88 emission, which is inconsistent with the n_e values inferred from the optical [O II], [S II], or [Cl III] lines (V. Leboutteiller et al. 2012). These optical diagnostics have higher critical densities and therefore likely trace more compact regions than [O III] 88.

The results indicate that the [O III] line ratios of COS-2987 cannot be reproduced by a simple model of homogeneous ionized gas with uniform temperature and density. In Section 5, we discuss two possible origins for this discrepancy.

5. Discussion

The FIR-to-optical [O III] line ratio diagnostics presented in the left panel of Figure 3 demonstrate that the observed values in COS-2987 cannot be explained by a homogeneous ionized gas with a single set of electron density and temperature. This discrepancy highlights the need to explore more complex scenarios for the ISM. In the following subsections, we discuss two possible origins of this tension: (i) the presence of inhomogeneously distributed dust within the ISM (Section 5.1); and (ii) a density-stratified ionized ISM structure (Sections 5.2 and 5.3).

5.1. Inhomogeneously Distributed Dust

One possibility to explain the observed [O III] line ratios could be an inhomogeneous dust distribution. This idea is suggested by ISM studies of local dwarf galaxies using rest-frame optical to FIR emission lines (e.g., Y. Chen et al. 2023, 2024; N. Kumari et al. 2024).

Y. Chen et al. (2024) analyzed both optical and FIR emission lines of [O III] (4364, 5008 Å and 88 μm) and [N II] (5755, 6583 Å and 122 μm) in Haro 3, to estimate both

²⁷ See also the “Data Calibration Considerations” in the JWST User Documentation: <https://jwst-docs.stsci.edu/jwst-calibration-status/jwst-absolute-flux-calibration#gsc.tab=0>.

²⁸ <https://almascience.eso.org/documents-and-tools/cycle6/alma-proposers-guide>

²⁹ In MACS0416-Y1, the NIRSpec prism mode does not spectrally resolve [O III] 4364 and H γ , but the authors were able to decompose these line fluxes based on the Balmer decrement obtained from H α and H β .

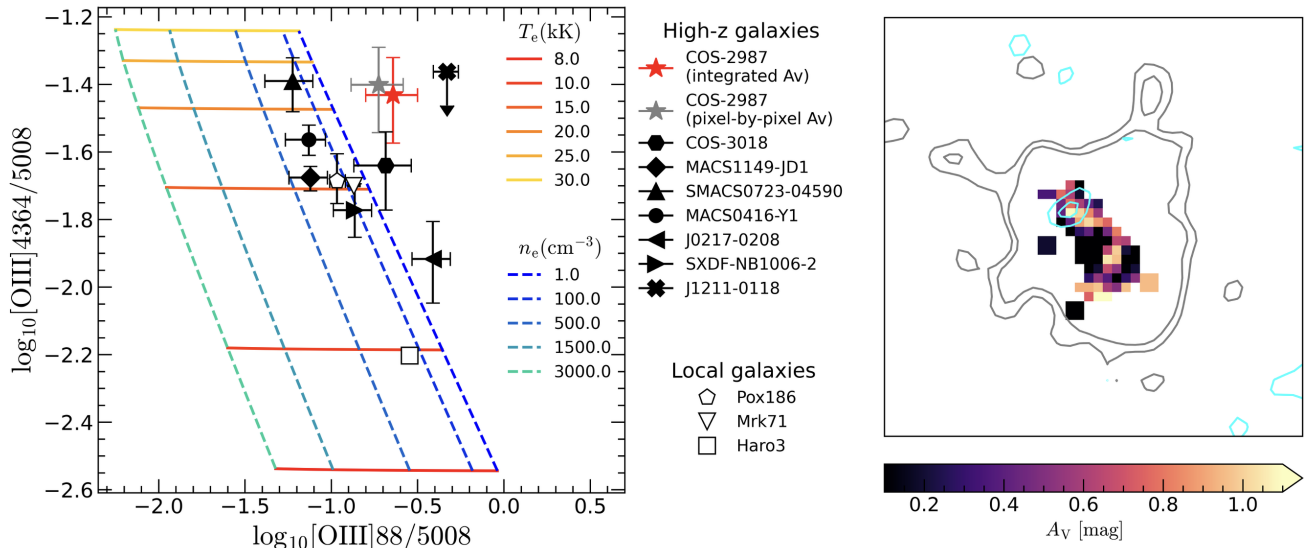


Figure 3. Left: diagnostic diagram of the [O III] line ratios overlaid with T_e - n_e model grids generated using P_YNeB (V. Luridiana et al. 2015). The red star indicates the observed [O III] line ratios of COS-2987 (Table 1). The gray star shows the ratios dust-corrected on a pixel-by-pixel basis using the A_V map shown in the right panel (Section 5.1). The black filled symbols represent high- z star-forming galaxies (J. Witstok et al. 2022; M. Stiavelli et al. 2023; S. Fujimoto et al. 2024; A. Harshan et al. 2024; Y. Harikane et al. 2025b), where the optical [O III] data are obtained from NIRSpc/IFS for COS-2987, COS-3018, SXDF-NB1006-2, J0217-0208, and J1211-0118 and from NIRSpc/MOS for the remaining galaxies. The open symbols represent local dwarf galaxies (Y. Chen et al. 2023, 2024; N. Kumari et al. 2024). The [O III] line ratios of COS-2987 lie outside the model grids, indicating that they cannot be reproduced by a homogeneous ionized gas with a single set of electron temperature and density. Right: A_V map derived from the $H\alpha/H\beta$ ratio, constructed within the 3σ regions of both the $H\alpha$ and $H\beta$ integrated intensity maps after the Voronoi binning (M. Cappellari & Y. Copin 2003; M. Cappellari 2009). The gray and cyan contours indicate the [O III] 5008 and [O III] 4364 integrated intensity maps, respectively, at the 2σ and 3σ levels.

electron temperatures and chemical abundance ratios. They found a significant discrepancy between the N^+/H^+ and N^+/O^{++} ratios derived from the optical and FIR [N II] lines, which they interpreted as evidence for the strong attenuation of optical lines due to inhomogeneously distributed dust.

In Y. Chen et al. (2024), the dust extinction correction was applied using the Balmer decrement measured from spatially integrated fluxes. However, if dust is distributed inhomogeneously within the galaxy, such integrated measurements would be biased toward regions with less dust extinction, leading to an underestimation of the true dust extinction.

If this hypothesis holds for COS-2987, the intrinsic [O III] 5008 and 4364 fluxes would be underestimated. Equivalently, the intrinsic [O III] 88/5008 and [O III] 4364/5008 ratio would be overestimated, potentially affecting the derived ISM physical properties. We test this hypothesis for COS-2987 as follows.

First, we generate an A_V map from the PSF-matched $H\alpha/H\beta$ ratio map within the 3σ regions of both line-intensity maps (the right panel of Figure 3). We apply Voronoi pixel binning (M. Cappellari & Y. Copin 2003; M. Cappellari 2009) to the integrated intensity maps of $H\beta$ and $H\alpha$ in order to optimize the signal-to-noise ratio in each pixel. The observed [O III] 4364 and [O III] 5008 intensity maps are then corrected for dust extinction on a pixel-by-pixel basis using the resulting A_V map.³⁰ Outside the region where the A_V map is not reliably

defined (i.e., where either $H\alpha$ or $H\beta$ is not detected above 3σ), we assume $A_V = 0$ for simplicity.

We measure the total dust-corrected [O III] 5008 and [O III] 4364 fluxes in a similar manner to the observed total fluxes (Section 2.1). We perform isophotal photometry on both dust-corrected line-intensity maps, where we use the 2σ isophotal aperture defined in the [O III] 5008 map (the outermost gray contour in the right panel of Figure 3). Then, we apply a 10% aperture correction (see Section 2.1) to both line flux values.

Finally, we estimate the pixel-by-pixel dust-corrected [O III] 4364/5008 and [O III] 88/5008 ratios, represented by a gray star in the left panel of Figure 3. As a result, we find that the [O III] 4364/5008 and [O III] 88/5008 ratios change by factors of ~ 1.07 and ~ 0.82 , respectively. However, even after this correction, the integrated [O III] ratios of COS-2987 still cannot be explained by a homogeneous ionized gas with densities comparable to those inferred from the [O II] lines.

We therefore conclude that the integrated [O III] ratios cannot be reproduced by an ISM characterized by a single set of electron density and temperature, even after accounting for the spatial structure of dust attenuation. This supports the view that inhomogeneously distributed dust is not the primary cause of the observed discrepancy in the [O III] line ratios of COS-2987.

5.2. Evidence for a Density-stratified Ionized ISM

A common assumption in deriving nebular physical parameters is that all emission lines originate from a homogeneous ionized gas with uniform electron density and temperature (see L. J. Kewley et al. 2019 and references therein). However, the critical density of [O III] 88 ($n_{e,\text{crit}} = 510 \text{ cm}^{-3}$) is approximately 3–4 orders of magnitude lower than those of [O III] 4364 ($3.0 \times 10^6 \text{ cm}^{-3}$) and [O III]

³⁰ We note that the [O III] 4364 detection region (the cyan contours in Figure 3) is smaller than the A_V map coverage. The dust extinction correction is applied even to low-significance pixels in the [O III] 4364 map. This could result in an underestimation of the dust-corrected [O III] 4364 flux and thus of the [O III] 4364/5008 ratio. Nevertheless, even if the ratio is underestimated, the true value would shift upward along the vertical axis in Figure 3, which does not alter our conclusion.

5008 ($6.8 \times 10^5 \text{ cm}^{-3}$; e.g., D. E. Osterbrock & G. J. Ferland 2006; B. T. Draine 2011). This large difference in critical densities suggests that the [O III] 88, [O III] 5008, and [O III] 4364 lines may originate from physically distinct ionized-gas conditions with different densities and temperatures.

We tested this possibility by examining the spatial and kinematic distributions of the [O III] 5008 and [O III] 88 lines. As shown in Figure B2 (Appendix B), the radial profiles of the two lines are consistent within uncertainties, indicating no significant spatial segregation at the current ALMA resolution. Similarly, Figure C1 in Appendix C shows that the spectral profiles of the two lines are broadly consistent, although the [O III] 88 line appears marginally broader. These results do not provide evidence for spatial or kinematic separation between the emitting regions at the given spatial and spectral resolutions of the current data. Moreover, we do not find any velocity components that are detected in the [O III] 88 line but absent from the [O III] 5008 line, which would otherwise be expected if dust attenuation played a major role. This further supports our conclusion in Section 5.1 that inhomogeneously distributed dust is not the primary cause of the observed discrepancy.

Motivated by the large differences in critical densities, we explore the possibility that the ionized gas in COS-2987 consists of multiple components with different electron densities and temperatures (i.e., a density-stratified ionized ISM). Although no significant spatial or kinematic offsets are observed, these findings do not rule out the presence of physically distinct gas. While comprehensive models for ionized gas with multiple physical conditions, such as MULTIGRIS (V. Leboutteiller & L. Ramambason 2022; L. Ramambason et al. 2022), are available, we adopt a simplified two-component toy model that focuses on three emission lines from doubly ionized oxygen: [O III] 4364, [O III] 5008, and [O III] 88. A similar analysis has been independently conducted for galaxies at $z = 6-9$ by Y. Harikane et al. (2025b). By limiting the number of free parameters, our aim is to identify the key physical conditions responsible for the observed line ratios.

In a two-component ionized-gas model, the luminosity of a given emission line (L_{line} , where “line” refers to [O III] 4364, [O III] 5008, or [O III] 88) can be expressed as

$$L_{\text{line}} = \left(\frac{\epsilon_{\text{line},1}}{\text{erg}} \text{ s}^{-1} \text{ cm}^{-3} \right) \left(\frac{V_1}{\text{cm}^3} \right) + \left(\frac{\epsilon_{\text{line},2}}{\text{erg}} \text{ s}^{-1} \text{ cm}^{-3} \right) \left(\frac{V_2}{\text{cm}^3} \right), \quad (3)$$

where $\epsilon_{\text{line},i}$ and V_i ($i = 1$ or 2) are the volume emissivity and the volume of each ionized-gas component, respectively. The emissivity $\epsilon_{\text{line},i}$ is given by

$$\epsilon_{\text{line},i} = \left(\frac{\Lambda_{\text{line},i}(n_{e,i}, T_{e,i})}{\text{erg}} \text{ s}^{-1} \text{ cm}^3 \right) \left(\frac{n_{e,i}}{\text{cm}^{-3}} \right) \left(\frac{n_{\text{O}^{++},i}}{\text{cm}^{-3}} \right), \quad (4)$$

where $\Lambda_{\text{line},i}$ is the cooling rate, and $n_{\text{O}^{++},i}$ is the number density of doubly ionized oxygen. We calculate $\Lambda_{\text{line},i}$ for each line using PyNeb (V. Luridiana et al. 2015), by assuming specific values of $n_{e,i}$ and $T_{e,i}$. We assume $n_{\text{O}^{++},i} = n_{e,i} \times 10^{-4}$, corresponding to $\text{O}^{++}/\text{H}^+ = 10^{-4}$ (i.e., $12 + \log(\text{O}^{++}/\text{H}^+) = 8$). The aim of this analysis is not to determine the best-fit parameters, but rather to assess whether

the observed [O III] luminosity ratios can be reproduced within the framework of a density-stratified ionized ISM.

In principle, the line luminosity ratios predicted by the two-component model can be expressed as a linear combination of the ratios corresponding to the individual components. Accordingly, in the top left panel of Figure 4, which is the same as Figure 3 but shown with linear scales on both axes, hot and dense gas (component 1) and relatively cool and diffuse gas (component 2) reside on the model grid representing a homogeneous ionized medium. The composite (i.e., global) line ratios are therefore expected to lie along the straight line connecting these two components.

We find that the observed [O III] line ratios are well reproduced by a model consisting of component 1 with $(T_{e,1}, n_{e,1}) = (26,000 \text{ K}, 500 \text{ cm}^{-3})$ and component 2 with $(T_{e,2}, n_{e,2}) = (8000 \text{ K}, 50 \text{ cm}^{-3})$. The components 1 and 2 are marked by the dark red and orange squares in the top left panel of Figure 4. As shown in the figure, the observed line ratios (indicated by the red star) can be reproduced by a linear combination of the two components with an appropriate volume ratio. We also note that other sets of physical conditions could reproduce the observed line ratios, such as a higher T_e for component 1 and a higher n_e for component 2. The top right panel of Figure 4 shows the predicted line ratios of the two-component model as a function of the volume ratio V_1/V_2 , with $T_{e,1}$, $n_{e,1}$, $T_{e,2}$, and $n_{e,2}$ held fixed. By comparing the model predictions with the observed values of [O III] 88/5008 and [O III] 4364/5008, we derive a volume ratio of $V_1/V_2 \sim 1/300$. The corresponding mass ratio of the two gas components is $M_1/M_2 \sim 1/30$, where the mass of each component is calculated as $M_i = n_{e,i}V_i$.

We stress again that the specific combination of the T_e , n_e , and V_1/V_2 parameters presented above is not a unique solution. Nevertheless, our two-component model successfully reproduces both the observed [O III] 88/5008 and [O III] 4364/5008 ratios simultaneously, which cannot be achieved by a commonly assumed homogeneous gas. We also note that the observed [O II] 3727, 3730 emission likely originates from a different ionization phase not included in our current model. One possible explanation is the presence of a third component with lower ionization and relatively high density, perhaps located at the surface of H I gas clouds in the galaxy. Exploring this additional phase is beyond the scope of the present work, but it will be an important direction for future modeling efforts.

5.3. Interpretation of the the Density-stratified Ionized ISM

The bottom panel of Figure 4 provides a schematic illustration of the density-stratified ionized ISM scenario. In this framework, component 1 corresponds to compact, dense, and high-temperature ionized regions associated with young massive stars or stellar clusters. Such regions are expected to be more common in high- z galaxies (M. Mingozi et al. 2022; M. W. Topping et al. 2025). The relatively cool and diffuse gas (component 2) is expected to surround the component 1 regions, because their volumes are different by a factor of ~ 300 . The diffuse and extended gas component may originate from hydrogen-ionizing photons—i.e., Lyman continuum (LyC) photons—leaking from dense high-temperature H II regions (component 1), resembling the so-called “picket-fence model” (T. M. Heckman et al. 2011; E. Leitet et al. 2013). This scenario is supported by observations of nearby massive

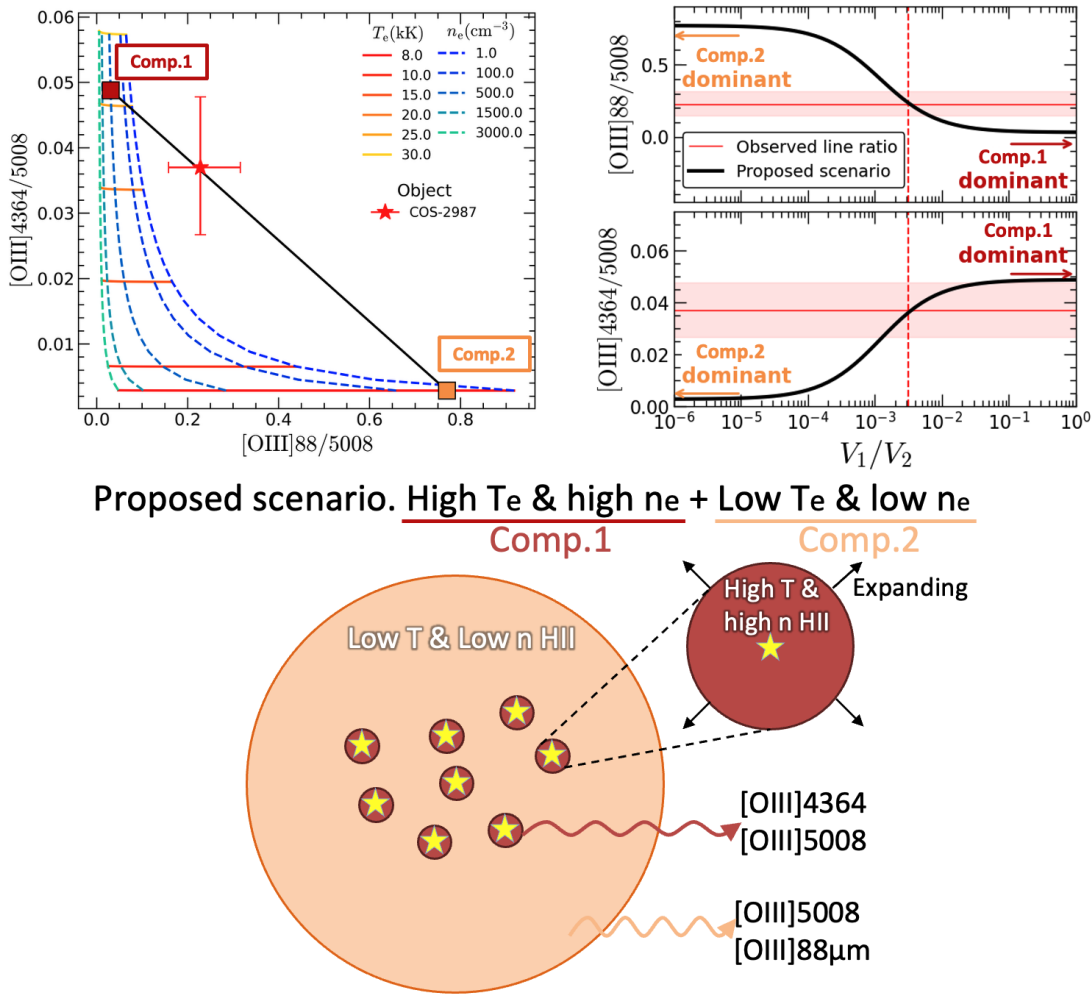


Figure 4. Top left: the same as the left panel of Figure 3 but shown with linear scales on both axes. The two squares correspond to the two gas components: the dark red square indicates component 1, with $(T_e, n_e) = (26,000 \text{ K}, 500 \text{ cm}^{-3})$, and the orange square indicates component 2, with $(T_e, n_e) = (8000 \text{ K}, 50 \text{ cm}^{-3})$. The observed line ratios of COS-2987 (red star) can be explained by an ISM composed of these two components, mixed at an appropriate volume ratio and represented by the line connecting the two squares. Top right: $[\text{O III}]_{88}/5008$ and $[\text{O III}]_{4364}/5008$ luminosity ratios as a function of volume ratio V_1/V_2 in our two-component model. The black curves show the predicted ratios from the model. The horizontal solid lines and shaded regions indicate the observed ratios and their 1σ uncertainties, respectively. The observed values are reproduced when $V_1 : V_2 \sim 1 : 300$ (vertical dashed lines). Bottom: schematic illustration of our proposed two-component gas scenario. Hot and dense H II regions around young massive stars or clusters (component 1) are surrounded by relatively cool and diffuse H II regions (component 2). From the perspective of pressure balance, the component 1 gas is expected to be expanding. The $[\text{O III}]_{4364}$ and $[\text{O III}]_{88}$ emissions arise primarily from the component 1 and 2 regions, respectively, while both components contribute to the $[\text{O III}]_{5008}$ emission.

star-forming regions: AKARI observations of 30 Doradus (M. Kawada et al. 2011) and Herschel/PACS observations of LMC-N11 (V. Leboutellier et al. 2012) revealed spatially extended $[\text{O III}]_{88}$ emission beyond the regions expected from the number of massive stars, likely due to a clumpy low-density medium that allows ionizing photons to propagate over large scales. Similarly, the modeling of the Herschel Dwarf Galaxy Survey (D. Cormier et al. 2015, 2019; L. Ramambason et al. 2022) also requires such a high-ionization, low-density component to reproduce the observed $[\text{O III}]_{88}$ flux. Such porous conditions would facilitate the leakage of LyC photons into the surrounding medium, relevant to the study of cosmic reionization (e.g., D. Cormier et al. 2019; L. Ramambason et al. 2022; M. Hagimoto et al. 2025).

Indeed, the detection of Ly α emission from COS-2987 at $z \sim 6.8$ (N. Laporte et al. 2017), prior to the completion of cosmic reionization, supports the presence of clear sight lines that facilitate LyC escape. We refer readers to the estimate of the LyC photon escape fraction for COS-2987 presented by

K. Mawatari et al. (2025). Using the analytic prescription of N. Choustikov et al. (2024), which incorporates parameters such as the O32 ratio ($[\text{O III}]_{4960,5008}/[\text{O II}]_{3727,3730}$) and H β luminosity, K. Mawatari et al. (2025) obtained a nonzero escape fraction of $f_{\text{esc}} = 5_{-5}^{+8}\%$. This estimate is consistent with the high $[\text{O III}]_{88 \mu\text{m}}$ -to- $[\text{C II}]_{158 \mu\text{m}}$ luminosity ratio of ≈ 6 in COS-2987 (J. Witstok et al. 2022). Based on the empirical relation proposed by R. Ura et al. (2023),³¹ we infer $f_{\text{esc}} \approx 4\% - 14\%$. Taken together, the results for COS-2987, along with similar trends in other high- z galaxies (Figure 3), may hint that high- z ALMA $[\text{O III}]_{88 \mu\text{m}}$ emitters—with potentially porous ionized-gas structures—contributed to cosmic reionization.

³¹ R. Ura et al. (2023) combined two positive correlations: (i) between the optical O32 ratio and f_{esc} ; and (ii) between the optical O32 ratio and the $[\text{O III}]_{88 \mu\text{m}}$ -to- $[\text{C II}]_{158 \mu\text{m}}$ luminosity ratio, thereby obtaining a correlation between the $[\text{O III}]_{88 \mu\text{m}}$ -to- $[\text{C II}]_{158 \mu\text{m}}$ ratio and f_{esc} .

To account for the extremely high electron temperature ($T_e \sim 20,000$ K) and the resulting strong [O III] 4364 emission of component 1, we note that one speculative possibility is the presence of an extreme stellar population, such as very massive stars (VMSs, with $M \gtrsim 150, M_\odot$; P. A. Crowther et al. 2010; J. S. Vink et al. 2015). Future follow-up observations in the rest-frame UV may provide useful clues, by examining spectral features that could be indicative of VMSs, such as an enhanced N/O ratio and a strong He II 1640 equivalent width (J. S. Vink 2023; P. Senchyna et al. 2024; A. Upadhyaya et al. 2024).

6. Conclusions

In this Letter, we have investigated the ionized ISM of the $z = 6.8$ galaxy COS-2987 using JWST/NIRSpec IFS and ALMA spectroscopy. Our main conclusions are summarized as follows:

1. JWST/NIRSpec spectra revealed multiple rest-frame optical emission lines in COS-2987, including [O II] $\lambda\lambda$ 3727, 3730, [O III] 4364, [O III] $\lambda\lambda$ 4960, 5008, and [O III] 88 μm , as well as H α and H β (Figure 1; Table 1). Using only the JWST/NIRSpec lines, we derived an electron density of $n_e \sim 500 \text{ cm}^{-3}$ from the [O II] doublet, consistent with the redshift evolution trend of n_e reported in previous studies (Figure 2).
2. From the combination of optical and FIR [O III] lines, we constructed a diagnostic diagram based on the [O III] 88/[O III] 5008 and [O III] 4364/[O III] 5008 ratios. COS-2987 falls well outside the grid predicted by homogeneous models computed with PYNeb. Furthermore, a compilation of other high- z galaxies shows a similar behavior, in which the n_e values inferred from the two combinations of [O III], [O III] 88/[O III] 5008 and [O III] 4364/[O III] 5008, are systematically lower than those derived from optical diagnostics such as [O II]. This indicates that the discrepancy is likely a general trend and demonstrates that the assumption of a uniform ionized gas with a single set of electron density and temperature could not be valid in a large fraction of high- z galaxies with strong [O III] 88 (Figure 3).
3. We examined whether inhomogeneously distributed dust could explain the high [O III] 88/[O III] 5008 ratios. We conclude that a clumpy dust distribution is not the primary cause of the discrepancy (see Section 5.1 and the right panel of Figure 3).
4. Instead, we showed that the observations can be reproduced by invoking a density-stratified ionized ISM. A simple two-component ionized-gas toy model with $(T_e, n_e) \sim (26,000 \text{ K}, 500 \text{ cm}^{-3})$ and $(8000 \text{ K}, 50 \text{ cm}^{-3})$ successfully reproduces the observed [O III] ratios. We discussed a physical scenario for such stratification: porous ISM conditions in which LyC photons leak from dense regions into a low-density medium, akin to a ‘‘picket-fence’’ geometry (Sections 5.2 and 5.3; Figure 4).

In summary, these results highlight the complex ionized-gas structure of the star-forming galaxy COS-2987, which may reflect its clumpy and extended morphology (K. Mawatari et al. 2025). Given that such clumpy multicomponent stellar structures are not uncommon among high-redshift galaxies (e.g., Y. Harikane et al. 2025a; Y. Sugahara et al. 2025), a future systematic investigation into the ubiquity of the density-

stratified ionized ISM at high redshift would be of great interest. A more detailed modeling of the multicomponent ISM in a larger sample of high- z galaxies will be addressed in a forthcoming paper (Y. Sugahara et al. 2025, in preparation). Given their high critical densities, rest-frame UV emission lines such as O III] and C III] offer promising avenues for probing density stratification in high- z galaxies. In addition, high-angular-resolution observations with ALMA are essential for obtaining spatially resolved measurements of the electron temperature, electron density, and [O III] 88/5008 ratio, thereby enabling constraints on the structure and physical conditions of density-stratified ionized ISM.

Acknowledgments

We are grateful to an anonymous referee for valuable comments that have greatly improved the Letter. We thank Masami Ouchi, Yoshiaki Ono, and Kimihiko Nakajima for providing us with valuable comments on the presentations of the first author. We also acknowledge Joris Witstok, Fengwu Sun, Tohru Nagao, Hide Yajima, Hajime Fukushima, Nario Kuno, Shunsuke Honda, Asahi Hamada, Yuuki Takagishi, and Yuzuru Terui for insightful discussion. This Letter makes use of the following ALMA data: ADS/JAO.ALMA#2018.1.00429.S. ALMA is a partnership of ESO (representing its member states), NSF (USA), and NINS (Japan), together with NRC (Canada), MOST and ASIAA (Taiwan), and KASI (Republic of Korea), in cooperation with the Republic of Chile. The Joint ALMA Observatory is operated by ESO, AUI/NRAO, and NAOJ. This work has made use of data from the European Space Agency (ESA) mission Gaia (<https://www.cosmos.esa.int/gaia>), processed by the Gaia Data Processing and Analysis Consortium (DPAC, <https://www.cosmos.esa.int/web/gaia/dpac/consortium>). Funding for the DPAC has been provided by national institutions, in particular the institutions participating in the Gaia Multilateral Agreement. The Gaia data are retrieved from the JVO portal (<http://jvo.nao.ac.jp/portal>) operated by the NAOJ. This research has made use of NASA’s Astrophysics Data System. T.H. was supported by the Leading Initiative for Excellent Young Researchers, MEXT, Japan (HJH02007) and by JSPS KAKENHI grant Nos. 22H01258, 23K22529, and 25K00020. K.M. acknowledges financial support from JSPS through KAKENHI grant No. 20K14516. K.M. and A.K.I. are supported by JSPS KAKENHI grant No. 23H00131. J.A.-M., L.C., and S.A. acknowledge support by grant PIB2021-127718NB-100 from the Spanish Ministry of Science and Innovation/State Agency of Research MCIN/AEI/10.13039/501100011033 and by ‘‘ERDF: A way of making Europe.’’ J. A.-M. and C.B.-P. acknowledge support by grant PID2024-158856NA-I00 from the Spanish Ministry of Science and Innovation/State Agency of Research MCIN/AEI/10.13039/501100011033 and by ‘‘ERDF: A way of making Europe.’’ Y.N. acknowledges funding from JSPS KAKENHI grant No. 23KJ0728. A.C.G. acknowledges support by JWST contract B0215/JWST-GO-02926. Y.W.R. was supported by JSPS KAKENHI grant No. 23KJ2052. Y.F. acknowledges support from JSPS KAKENHI grant Nos. JP22K21349 and JP23K13149. M.H. was supported by JSPS KAKENHI grant No. 22KJ1598. The project that gave rise to these results received the support of a fellowship from the ‘‘la Caixa’’ Foundation (ID 100010434). The fellowship code is LCF/BQ/PR24/12050015. L.C. acknowledges support from grants

PID2022-139567NB-I00 and PIB2021-127718NB-I00 funded by the Spanish Ministry of Science and Innovation/State Agency of Research MCIN/AEI/10.13039/501100011033 and by “ERDF: A way of making Europe.” D.C. is supported by research grant PID2021-122603NB-C21 funded by the Ministerio de Ciencia, Innovación y Universidades (MI-CIU/FEDER), and the research grant CNS2024-154550 funded by MI-CIU/AEI/10.13039/501100011033. C.B.P. acknowledges the support of the Consejería de Educación, Ciencia y Universidades de la Comunidad de Madrid, through grant Nos. PEJ-2021-AI/TIC-21517 and PIPF-2023/TEC29505.

Software: scipy, astropy, PyNeb, photutils.

Appendix A PSF of the NIRSspec IFS Data Cube

To ensure that the line fluxes are measured from the same spatial region, we use a PSF-matched data cube, as described in K. Mawatari et al. (2025). Here, we briefly summarize the procedure used to create the PSF-matched data cube. To obtain an empirical PSF for the data cube, we analyzed observations of the A3V star 1808347 (2MASS J18083474+6927286) taken during the commissioning program (PID 1128; PI: N. Lützgendorf; T. Böker et al. 2023), using the same grating/filter combination (G395H/F290LP) as for COS-2987. The data reduction for the standard star was performed with the same JWST pipeline version and CRDS context as for COS-2987.

From the data cube of the A3V star, we generated PSF images at the wavelengths corresponding to the emission lines detected in COS-2987. We then created convolution kernels to homogenize all PSFs to match the PSF at $5.125 \mu\text{m}$, corresponding to the observed wavelength of $\text{H}\alpha$ in COS-2987, which has the largest FWHM of $0''.21$ among the detected lines.

Appendix B Radial Profiles of [O III] 5008 and [O III] 88

We examined the spatial distributions of the [O III] 5008 and [O III] 88 emission lines, as shown in Figures B1 and B2. In Figure B1, we present the integrated intensity maps of both lines, where the [O III] 5008 map has been convolved to match the ALMA beam size ($0''.8 \times 0''.6$). To quantitatively assess the spatial difference, we compare the radial profiles of [O III] 5008 and [O III] 88 in Figure B2. The blue and red lines with shaded regions represent the radial profiles of [O III] 5008 and [O III] 88, respectively. The two emission lines exhibit consistent radial distributions within the uncertainties, indicating that there is no significant evidence of spatial separation between the two lines at the current ALMA resolution.

We note, however, that this result does not exclude the possibility that future high-angular-resolution observations could reveal subtle morphological differences between the [O III] 5008 and [O III] 88 emissions.

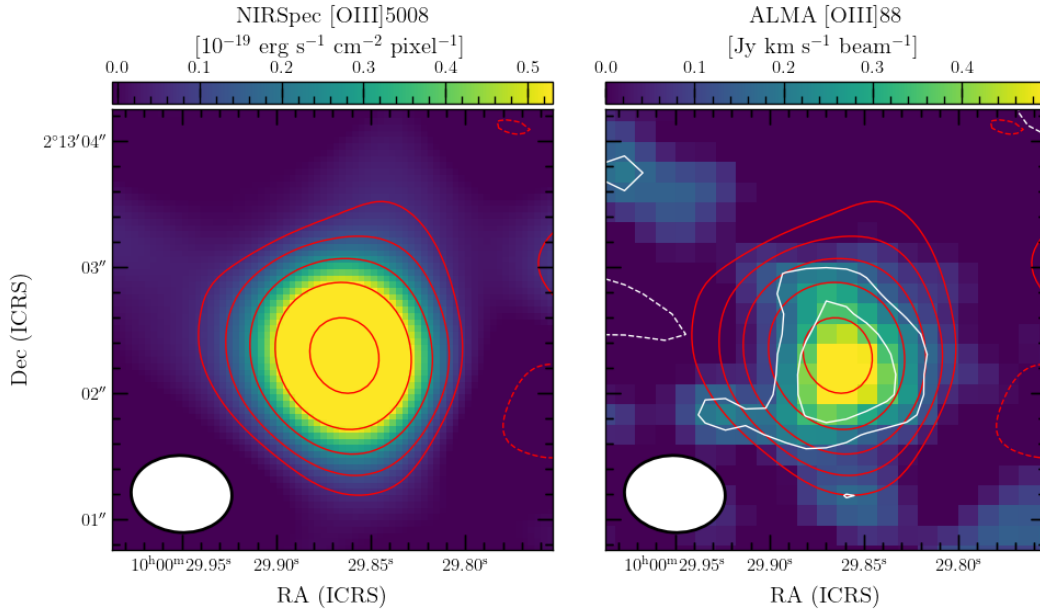


Figure B1. Left: integrated intensity map of the NIRSspec [O III] 5008 emission, after convolution to match the ALMA beam size ($0''.80 \times 0''.61$). The red contours show the $\pm 2\sigma$ significance levels ($n = 1, 2, 3, \dots$), where $\sigma = 1.16 \times 10^{-20} \text{ erg s}^{-1} \text{ cm}^{-2} \text{ pixel}^{-1}$. The orange circle at the bottom left indicates the FWHM of $0''.21$ at the observed wavelength of $\text{H}\alpha$ ($5.125 \mu\text{m}$). Right: integrated intensity map of the ALMA [O III] 88 emission. The white contours show the $\pm(2, 4, 6)\sigma$ significance levels, where $\sigma = 82.6 \text{ mJy beam}^{-1} \text{ km s}^{-1}$. Positive and negative contours are shown by the white solid and dashed lines, respectively. The white ellipse at the bottom left represents the synthesized beam size of $0''.80 \times 0''.61$.

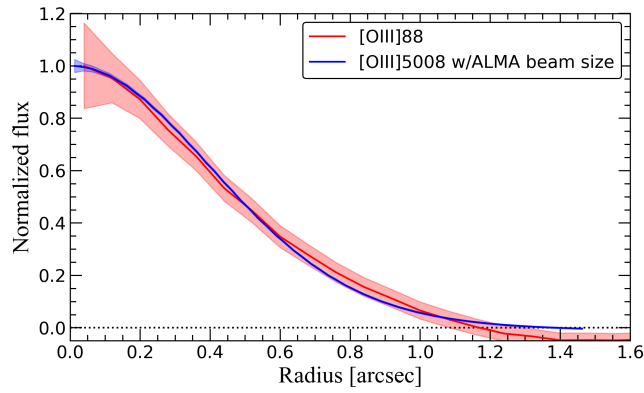


Figure B2. Radial profiles of the [O III] 5008 and [O III] 88 emission lines. The blue and red lines represent the profiles of [O III] 5008 and [O III] 88, respectively, with the shaded regions indicating their corresponding uncertainties.

Appendix C Line Profiles of [O III] 5008 and [O III] 88

We investigated potential differences in the line profiles between the [O III] 5008 and [O III] 88 emissions. Figure C1 shows the velocity profiles of [O III] 5008 and [O III] 88, represented by the blue and red lines, respectively. Fitting each line with a single Gaussian profile and correcting for instrumental broadening, we obtain $\text{FWHM}_{5008} = 146 \pm 2 \text{ km s}^{-1}$ and $\text{FWHM}_{88} = 239 \pm 45 \text{ km s}^{-1}$. These values are consistent within $\sim 2\sigma$, although the [O III] 88 line appears marginally broader.

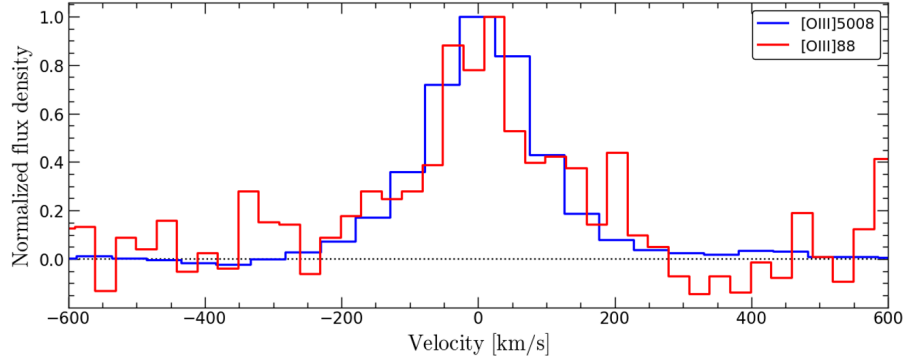


Figure C1. Comparison of the velocity profiles of the [O III] 5008 and [O III] 88 emission lines. The blue and red lines represent the profiles of [O III] 5008 and [O III] 88, respectively, normalized to their peak intensities.

ORCID iDs

Ken Mawatari  <https://orcid.org/0000-0003-4985-0201>
 Javier Álvarez-Márquez  <https://orcid.org/0000-0002-7093-1877>
 Takuya Hashimoto  <https://orcid.org/0000-0002-0898-4038>
 Yuma Sugahara  <https://orcid.org/0000-0001-6958-7856>
 Rui Marques-Chaves  <https://orcid.org/0000-0001-8442-1846>
 Akio K. Inoue  <https://orcid.org/0000-0002-7779-8677>
 Luis Colina  <https://orcid.org/0000-0002-9090-4227>
 Santiago Arribas  <https://orcid.org/0000-0001-7997-1640>
 Carmen Blanco-Prieto  <https://orcid.org/0009-0005-5448-5239>
 Yurina Nakazato  <https://orcid.org/0000-0002-0984-7713>
 Naoki Yoshida  <https://orcid.org/0000-0001-7925-238X>
 Tom J. L. C. Bakx  <https://orcid.org/0000-0002-5268-2221>
 Daniel Ceverino  <https://orcid.org/0000-0002-8680-248X>
 Luca Costantin  <https://orcid.org/0000-0001-6820-0015>
 Alejandro Crespo Gómez  <https://orcid.org/0000-0003-2119-277X>
 Masato Hagimoto  <https://orcid.org/0000-0001-8083-5814>
 Hiroshi Matsuo  <https://orcid.org/0000-0003-3278-2484>
 Wataru Osone  <https://orcid.org/0009-0008-8424-100X>
 Yi W. Ren  <https://orcid.org/0000-0002-6510-5028>
 Yoshinobu Fudamoto  <https://orcid.org/0000-0001-7440-8832>
 Miguel Pereira-Santaella  <https://orcid.org/0000-0002-4005-9619>
 Yoichi Tamura  <https://orcid.org/0000-0003-4807-8117>

References

- Abdurro'uf, Larson, R. L., Coe, D., et al. 2024, *ApJ*, 973, 47
 Álvarez-Márquez, J., Crespo Gómez, A., Colina, L., et al. 2025, *A&A*, 695, A250
 Arribas, S., Perna, M., Rodríguez Del Pino, B., et al. 2024, *A&A*, 688, A146
 Asplund, M., Grevesse, N., Sauval, A. J., & Scott, P. 2009, *ARA&A*, 47, 481
 Bakx, T., & Conway, J. 2024, *ALMA Memo Series*, 627, 2024
 Bakx, T. J. L. C., Tamura, Y., Hashimoto, T., et al. 2020, *MNRAS*, 493, 4294
 Böker, T., Arribas, S., Lützgendorf, N., et al. 2022, *A&A*, 661, A82
 Böker, T., Beck, T. L., Birkmann, S. M., et al. 2023, *PASP*, 135, 038001
 Bushouse, H., Eisenhamer, J., Dencheva, N., et al. 2024, JWST Calibration Pipeline, v1.14.0, Zenodo, doi:10.5281/zenodo.6984365
 Campbell, A., Terlevich, R., & Melnick, J. 1986, *MNRAS*, 223, 811
 Cappellari, M. 2009, arXiv:0912.1303
 Cappellari, M., & Copin, Y. 2003, *MNRAS*, 342, 345
 CASA Team, Bean, B., Bhatnagar, S., et al. 2022, *PASP*, 134, 114501
 Chen, Y., Jones, T., Sanders, R., et al. 2023, *NatAs*, 7, 771
 Chen, Y., Jones, T., Sanders, R. L., et al. 2024, arXiv:2405.18476
 Choustikov, N., Katz, H., Saxena, A., et al. 2024, *MNRAS*, 529, 3751
 Cormier, D., Abel, N. P., Hony, S., et al. 2019, *A&A*, 626, A23
 Cormier, D., Madden, S. C., Lebouteiller, V., et al. 2015, *A&A*, 578, A53
 Crowther, P. A., Schnurr, O., Hirschi, R., et al. 2010, *MNRAS*, 408, 731
 Curti, M., Maiolino, R., Curtis-Lake, E., et al. 2024, *A&A*, 684, A75
 Davies, R. L., Förster Schreiber, N. M., Genzel, R., et al. 2021, *ApJ*, 909, 78
 Dinerstein, H. L., Lester, D. F., & Werner, M. W. 1985, *ApJ*, 291, 561
 Draine, B. T. 2011, *Physics of the Interstellar and Intergalactic Medium* (Princeton, NJ: Princeton Univ. Press) <https://press.princeton.edu/books/paperback/9780691122144/physics-of-the-interstellar-and-intergalactic-medium>
 Fujimoto, S., Ouchi, M., Nakajima, K., et al. 2024, *ApJ*, 964, 146
 Gardner, J. P., Mather, J. C., Abbott, R., et al. 2023, *PASP*, 135, 068001
 Gordon, K. D., Clayton, G. C., Misselt, K. A., Landolt, A. U., & Wolff, M. J. 2003, *ApJ*, 594, 279
 Hagimoto, M., Tamura, Y., Inoue, A. K., et al. 2025, *ApJ*, 990, 29
 Harikane, Y., Inoue, A. K., Ellis, R. S., et al. 2025a, *ApJ*, 980, 138
 Harikane, Y., Ouchi, M., Inoue, A. K., et al. 2020, *ApJ*, 896, 93
 Harikane, Y., Sanders, R. L., Ellis, R., et al. 2025b, arXiv:2505.09186
 Harshan, A., Tripodi, R., Martis, N. S., et al. 2024, *ApJL*, 977, L36
 Hashimoto, T., Álvarez-Márquez, J., Fudamoto, Y., et al. 2023, *ApJL*, 955, L2
 Hashimoto, T., Laporte, N., Mawatari, K., et al. 2018, *Natur*, 557, 392
 Heckman, T. M., Borthakur, S., Overzier, R., et al. 2011, *ApJ*, 730, 5
 Inoue, A. K., Tamura, Y., Matsuo, H., et al. 2016, *Sci*, 352, 1559
 Isobe, Y., Ouchi, M., Nakajima, K., et al. 2023, *ApJ*, 956, 139
 Ji, X., Übler, H., Maiolino, R., et al. 2024, *MNRAS*, 535, 881
 Jones, T., Sanders, R., Roberts-Borsani, G., et al. 2020, *ApJ*, 903, 150
 Kawada, M., Takahashi, A., Yasuda, A., et al. 2011, *PASJ*, 63, 903
 Kewley, L. J., Nicholls, D. C., Sutherland, R., et al. 2019, *ApJ*, 880, 16
 Killi, M., Watson, D., Fujimoto, S., et al. 2023, *MNRAS*, 521, 2526
 Kumari, N., Smit, R., Leitherer, C., et al. 2024, *MNRAS*, 529, 781
 Laporte, N., Nakajima, K., Ellis, R. S., et al. 2017, *ApJ*, 851, 40
 Laseter, I. H., Maseda, M. V., Curti, M., et al. 2024, *A&A*, 681, A70
 Lebouteiller, V., Cormier, D., Madden, S. C., et al. 2012, *A&A*, 548, A91
 Lebouteiller, V., & Ramambason, L. 2022, *A&A*, 667, A34
 Leitet, E., Bergvall, N., Hayes, M., Linné, S., & Zackrisson, E. 2013, *A&A*, 553, A106
 Luridiana, V., Morisset, C., & Shaw, R. A. 2015, *A&A*, 573, A42
 Marconcini, C., D'Eugenio, F., Maiolino, R., et al. 2024, *MNRAS*, 533, 2488
 Marshall, M. A., Perna, M., Willott, C. J., et al. 2023, *A&A*, 678, A191
 Mawatari, K., Costantin, L., Usui, M., et al. 2025, arXiv:2507.02053
 Mingozi, M., James, B. L., Arellano-Córdova, K. Z., et al. 2022, *ApJ*, 939, 110
 Morishita, T., Stiavelli, M., Grillo, C., et al. 2024, *ApJ*, 971, 43
 Nakajima, K., Ouchi, M., Isobe, Y., et al. 2023, *ApJS*, 269, 33
 Nakazato, Y., Yoshida, N., & Ceverino, D. 2023, *ApJ*, 953, 140
 Osterbrock, D. E., & Ferland, G. J. 2006, *Astrophysics of Gaseous Nebulae and Active Galactic Nuclei* (Sausalito, CA: Univ. Science Books)
 Perna, M., Arribas, S., Marshall, M., et al. 2023, *A&A*, 679, A89
 Posses, A. C., Aravena, M., González-López, J., et al. 2023, *A&A*, 669, A46
 Ramambason, L., Lebouteiller, V., Bik, A., et al. 2022, *A&A*, 667, A35
 Ren, Y. W., Fudamoto, Y., Inoue, A. K., et al. 2023, *ApJ*, 945, 69
 Rhoads, J. E., Wold, I. G. B., Harish, S., et al. 2023, *ApJL*, 942, L14
 Rigby, J. R., Vieira, J. D., Phadke, K. A., et al. 2025, *ApJ*, 978, 108
 Sanders, R. L., Shapley, A. E., Kriek, M., et al. 2016, *ApJ*, 816, 23
 Sanders, R. L., Shapley, A. E., Topping, M. W., Reddy, N. A., & Brammer, G. B. 2024, *ApJ*, 962, 24
 Schaerer, D., Marques-Chaves, R., Barrufet, L., et al. 2022, *A&A*, 665, L4
 Schlegel, D. J., Finkbeiner, D. P., & Davis, M. 1998, *ApJ*, 500, 525
 Scholtz, J., Curti, M., D'Eugenio, F., et al. 2025, *MNRAS*, 539, 2463
 Sekimoto, Y., Iizuko, Y., Satou, N., et al. 2008, in *Nineteenth Int. Symp. on Space Terahertz Technology*, ed. W. Wild (Charlottesville, VA: National Radio Astronomy Observatory), 253, <https://www.nrao.edu/meetings/issst/proceed/2008-Proceedings.pdf>
 Senchyna, P., Plat, A., Stark, D. P., et al. 2024, *ApJ*, 966, 92
 Smit, R., Bouwens, R. J., Carniani, S., et al. 2018, *Natur*, 553, 178
 Smit, R., Bouwens, R. J., Franx, M., et al. 2015, *ApJ*, 801, 122
 Stasińska, G. 1982, *A&AS*, 48, 299
 Stiavelli, M., Morishita, T., Chiaberge, M., et al. 2023, *ApJL*, 957, L18
 Sugahara, Y., Álvarez-Márquez, J., Hashimoto, T., et al. 2025, *ApJ*, 981, 135
 Tamura, Y., C. Bakx, T. J. L., Inoue, A. K., et al. 2023, *ApJ*, 952, 9
 Tokuoka, T., Inoue, A. K., Hashimoto, T., et al. 2022, *ApJL*, 933, L19
 Topping, M. W., Stark, D. P., Senchyna, P., et al. 2025, *ApJ*, 980, 225
 Übler, H., Maiolino, R., Curtis-Lake, E., et al. 2023, *A&A*, 677, A145
 Upadhyaya, A., Marques-Chaves, R., Schaerer, D., et al. 2024, *A&A*, 686, A185
 Ura, R., Hashimoto, T., Inoue, A. K., et al. 2023, *ApJ*, 948, 3
 Vink, J. S. 2023, *A&A*, 679, L9
 Vink, J. S., Heger, A., Krumholz, M. R., et al. 2015, *HiA*, 16, 51
 Welch, B., Olivier, G. M., Hutchison, T. A., et al. 2024, *ApJ*, 975, 196
 Witstok, J., Smit, R., Maiolino, R., et al. 2022, *MNRAS*, 515, 1751
 Wootten, A., & Thompson, A. R. 2009, *IEEEP*, 97, 1463
 Yang, S., & Lidz, A. 2020, *MNRAS*, 499, 3417
 Zavala, J. A., Castellano, M., Akins, H. B., et al. 2025, *NatAs*, 9, 155